minerals

MDPI

Article

Mineral Chemistry and Whole-Rock Analysis of Magnesian and Ferroan Granitic Suites of Magal Gebreel, South Eastern Desert: Clues for Neoproterozoic Syn- and Post-Collisional Felsic Magmatism

El Saeed R. Lasheen [1,*], Gehad M. Saleh [2], Amira El-Tohamy [2], Farrage M. Khaleal [2], Mabrouk Sami [3], Ioan V. Sanislav [4] and Fathy Abdalla [5,*]

[1] Geology Department, Faculty of Science, Al-Azhar University, Cairo 11884, Egypt
[2] Nuclear Materials Authority, El-Maadi, Cairo P.O. Box 530, Egypt
[3] Geosciences Department, College of Science, United Arab Emirates University, Al Ain 15551, United Arab Emirates
[4] Economic Geology Research Centre (EGRU), College of Science and Engineering, James Cook University, Townsville, QLD 4811, Australia
[5] College of Science, King Saud University, Riyadh 11451, Saudi Arabia
* Correspondence: elsaeedlasheen@azhar.edu.eg (E.S.R.L.); fabdalla@ksu.edu.sa (F.A.)

Abstract

The article provides a comprehensive analysis of the Magal Gebreel granitic suites (MGGs) using petrological (fieldwork, petrography, mineral chemistry, and bulk rock analysis) aspects to infer their petrogenesis and emplacement setting. Our understanding of the development of the northern portion of the Arabian Nubian Shield is significantly improved by the Neoproterozoic granitic rocks of the seldom studied MGGs in Egypt's south Eastern Desert. According to detailed field, mineralogical, and geochemical assessments, they comprise syn-collision (granodiorites) and post-collision (monzogranites, syenogranites, and alkali feldspar rocks). Granodiorite has strong positive Pb, notable negative P, Ti, and Nb anomalies, and is magnesian in composition. They have high content of LREEs (light rare-earth elements) compared to HREEs (heavy rare-earth elements) and clear elevation of LFSEs (low-field strength elements; K Rb, and Ba) compared to HFSEs (high-field strength elements; Zr and Nb), which are in accord with the contents of I-type granites from the Eastern Desert. In this context, the granodiorites are indicative of an early magmatic phase that probably resulted from the partial melting of high K-mafic sources in the subduction zone. Conversely, the post-collision rocks have low contents of Mg#, CaO, P_2O_5, MgO, Fe_2O_3, Sr, and Ti, and high SiO_2, Fe_2O_3/MgO, Nb, Ce, and Ga/Al, suggesting A-type features with ferroan affinity. Their P, Nb, Sr, Ba, and Ti negative anomalies are in accord with the findings for Eastern Desert granites of the A2-type. Furthermore, they exhibit a prominent negative anomaly in Eu and a small elevation of LREEs in relation to HREEs. The oxygen fugacity (fO_2) for the rocks under investigation can be calculated using the biotite chemistry. The narrow Fe/(Fe + Mg) ratio range (0.6–0.75) indicates that they crystallized under moderately oxidizing conditions between ~QFM +0.1 and QFM +1. The A-type rocks were formed by the partial melting of a tonalite source (underplating rocks) in a post-collisional environment during the late period of extension via slab delamination. The lithosphere became somewhat impregnated with particular elements as a result of the interaction between the deeper crust and the upwelling mantle.

Keywords: I- and A2-type magmatism; petrogenesis; mineral chemistry; geodynamic setting

Received: 5 June 2025
Revised: 25 June 2025
Accepted: 15 July 2025
Published: 17 July 2025

Citation: Lasheen, E.S.R.; Saleh, G.M.; El-Tohamy, A.; Khaleal, F.M.; Sami, M.; Sanislav, I.V.; Abdalla, F. Mineral Chemistry and Whole-Rock Analysis of Magnesian and Ferroan Granitic Suites of Magal Gebreel, South Eastern Desert: Clues for Neoproterozoic Syn- and Post-Collisional Felsic Magmatism. *Minerals* **2025**, *15*, 751. https://doi.org/10.3390/min15070751

1. Introduction

The Pan-African orogenic belt spans the Arabian Peninsula and a considerable portion of northern Africa. From East to West Gondwana, an accretionary orogenic belt formed, producing the Neoproterozoic crustal material of the Arabian-Nubian Shield (ANS). The Eastern Desert of the ANS and the greatest East African Orogen comprise the majority of the Neoproterozoic crystalline rocks [1–4]. In Egypt, these rocks (include accreted arc and ophiolites assemblages, Dokhan rocks, and various intrusive magmatism) cover over 100,000 km^2, particularly in South Sinai and the Eastern Desert. The southern sector of the Eastern Desert (ED) comprises the largest crystalline rocks, which are less studied due to absence of banded iron, Dokhan, Hammamat sediments, and roads made of asphalt [5]. The E-W of Yanbu-Allaqi-Gerf suture marks the boundary of the southern sector of the ED, which is characterized by abundant ophiolitic rocks [6]. According to Bonin [7], granite is the common igneous rock type in the upper continental crust of the Earth. Granites (differing in age, mineral content, and chemical components and can be found in a range of tectonic environments) make up almost 60% of the basement of Egypt's Nubian Shield [2,8–15]. Two types of granites were identified by Bentor [16]: younger (post-to-anorogenic granite; 600–475 Ma) and older syn (I-type)-to-late-orogenic granites (A-type; 880–610 Ma). The Eastern Desert of Egypt and across the ANS are examples of the youngest phase of felsic magmatism represented by A-type granites, which are divided into anorogenic (A1) and post-orogenic (A2) granites. According to Lundmark [17], the alkaline granite that results from the differentiation of alkali-basaltic magmas is the final phase of the younger rocks (A1-type), which date to approximately 540 Ma. The high level of silica, trace elements (Zr, Ce, Nb, Y, Ga, and REEs), and alkalis within A2-type granites make them a unique class of high-K calc-alkaline granite [18–21]. Additionally, their Ga/Al and Fe/Mg ratios are high, whereas their Ca and Sr concentrations are low [22,23]. The associations with significant mineral deposits make A-type granites distinctive. They are often associated with mineralization that is related to hydrothermal fluids. A-type granites are characterized by noticeable content of incompatible elements such as REEs, W, U, Th, Nb, and Sn. Granite has become a common decorative stone in recent years. They attracted a lot of attention because of their significant financial influence [24,25].

The aim of this research is to incorporate fieldwork, petrography, mineral chemistry, and bulk rock analysis of the seldom investigated Magal Gebreel granitic suites rocks in the ANS to infer and understand their petrogenesis, natural type, and geodynamic history. Additionally, we aim to elucidate the crustal contamination and fractionation processes of these rocks.

2. Methodology

Several trips were conducted to collect rock samples and investigate the geological highlights. Forty-two specimens were collected from the Magal Gebreel area, and thirty thin sections were cut out at the Nuclear Materials Authority (NMA) to determine their mineralogical distinctive features. In the Laboratory of Mettallogenic Prediction of Nonferrous Metals, Central South University, Changsha, China, using EPMA-170/1720H electron microprobes, the mineral chemistry was elucidated. A 15 kV accelerating voltage, a probe current between 10 and 20 nA, and a beam diameter of 2 to 3 μm were all used in the experimental setup. A blend of appropriate synthetic and natural standards for calibration purposes was also employed. The samples were subjected to geochemical investigations utilizing a Bruker S2 RANGER X-ray fluorescence. The studies comprised figuring out the amounts of minor elements (ppm) and main oxides (%) for the 23 samples. Three grams of fine powder was subjected to 1000 °C in order to estimate the loss on ignition (LOI). Inductively coupled plasma mass spectrometry (ICP-MS) was used to ac-

complish the REEs + Y concentrations at Kyushu University's Center, Japan. The analytical precision, as estimated by duplicate analyses, is between ±5% and ±10% for trace elements, between ±3% and ±7% for REEs, and superior to ±2% for main elements.

3. Field Observations

The crystalline rocks of the Gabal Magal Gebreel-Wadi Nagieb area, which constitute a part of the ANS, is situated in the southern region of Egypt's Eastern Desert, about 240 km southeast of Aswan, which covers about 255 km^2 (Figure 1). The topographic features are mainly controlled by the differences in lithology, structures, and erosional processes. The prominent peaks are Gabal Magal Gebreal granites (490 m) and Gebel Abu Swayel (375 m) above sea level.

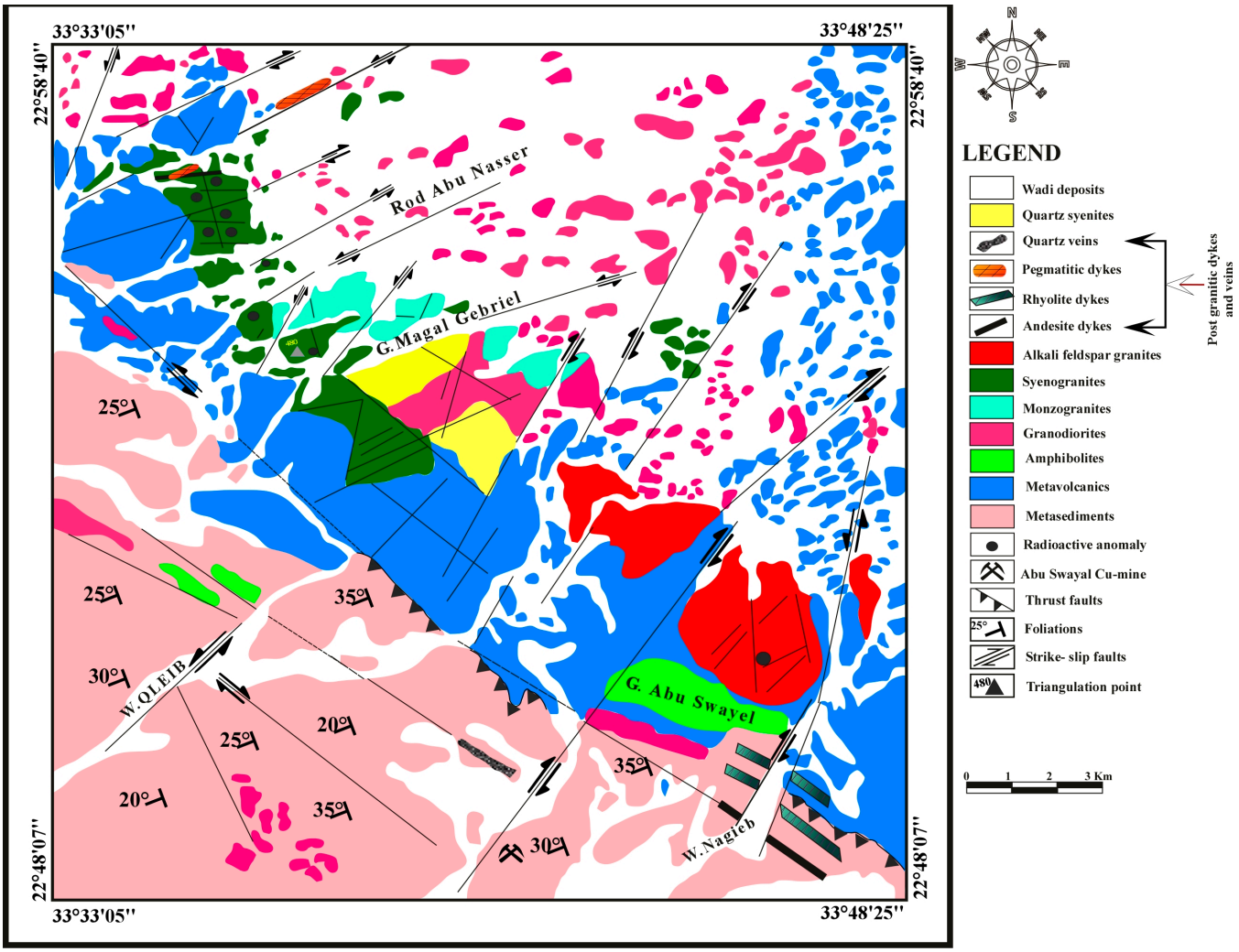

Figure 1. Geologic map of the Gabal Magal Gebreel-Wadi Nagieb area [26].

The study area comprises different types of igneous and metamorphic rocks, including metasedimentes, metavolcanics (basic and acidic), amphibolite rocks, younger and older granites, and dikes (acidic dikes and pegmatite) (Figure 2a). The metasedimentes exhibit foliations, laminations, and primary bedding, and are strongly tectonized (Figure 2b). They crop out in the southwestern mapped area as isolated masses. These rocks are intruded by metavolcanics, amphibolite rocks, and older granites with sharp contacts of Wadi Nagieb. The metavolcanics crop out in the eastern and center area under investigation as an elongated (with NW–SE) sheet forming low to moderate relief. They are represented by

metabasalt, metaandesite, and metarhyolite, which are invaded by younger granites. The amphibolites are (Gabal Abu Swayel) exposed at the southeastern side (covering a small area) of the investigated area. Their grains are fine-to-medium with a greenish gray to deep green color.

Figure 2. Field photographs showing: (**a**) panoramic view of the examined area with topography that is comparatively low-to-moderate, looking to the NE; (**b**) highly tectonized metasediments injected by felsic dike, looking NE; (**c**) younger granites reveal cavernous due to weathering products; (**d**) smooth surface as a result of weathering products; and (**e**) hematitization associated with high radioactive anomaly, looking NE.

The older granitoids crop out in the northern and extreme eastern sides of the investigated area. They injected the metasediments, metavolcanics, and younger granites. The topography that characterizes their exposure is comparatively low-medium, sheared, and shows intensive weathering products. The younger granites are fine-to-medium-grained with moderate-to-high topography (490 m. a.s.l.) and cover about 95 km^2 of the area. These rocks are deeply jointed and exhibit cavernous, exfoliation weathering, and bouldery appearance (Figure 2c,d). The field studies indicated that the hydrothermal processes have an impact on these granites, particularly near faults and zones of shear causing hematitization,

chloritization, and silicification zones (Figure 2e). These rocks are dissected by several felsic and mafic dikes, as well as quartz and pegmatite veins.

4. Results

4.1. Petrography

The mineralogy and textural properties were thoroughly described petrographically. Granodiorite, monzogranites, syenogranites, and alkali feldspar are the four major phases of MGGs, according to the modal analysis. Hypidiomorphic texture and medium-grained are the general features of granodiorites. In addition to accessory zircon mineral, it mainly contains plagioclase (40%–50%), quartz (20%–25%), orthoclase perthite (5%–10%), biotite (5%–10%), and amphibole (3%–5%). The primary mineral component of granodiorite, plagioclase, has an unclear surface as a result of saussuritization (Figure 3a). Hornblende is mostly transformed into opaque minerals and chlorite at the peripheral parts (Figure 3a,b). Biotite is identified as brown, elongated flaks, and somewhat chloritized flakes (Figure 3b). On the boundary between plagioclase and biotite, zircon is found as a euhedral crystal (Figure 3b).

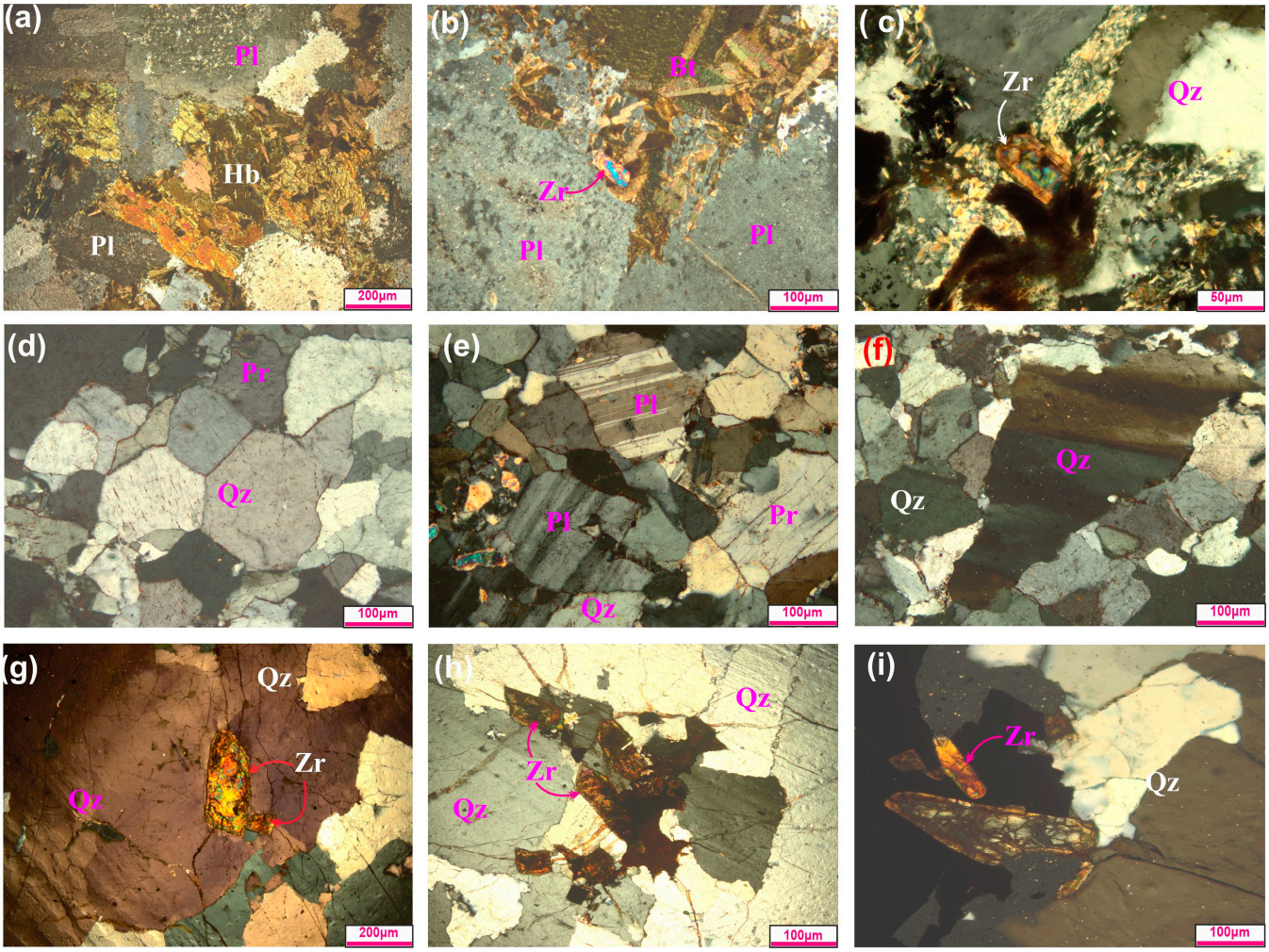

Figure 3. Microscopic photos of Magal Gebreel rocks showing: (**a**) deformed hornblende (Hb) associating biotite (Bt) flaks (granodiorite); (**b**) zircon (Zr) is enclosed in periphery of biotite (granodiorite); (**c**) metamictized zircon associated with sericite muscovite (monzogranite); (**d**) euhedral crystals of quartz (Qz) showing triple junction (syenogranite); (**e**) pristine albitic plagioclase (Pl) corroded by quartz crystals; (**f**) undulose quartz crystals (syenogranite); and (**g**–**i**) well-developed zircon crystals enclosed in quartz grain (alkali feldspar granites).

Monzogranite is medium-grained and made up of K-feldspar, quartz, and plagioclase, with trace amounts of muscovite and biotite. K-feldspar (32–35 vol.%) is of subhedral to anhedral crystal of orthoclase perthite. Sericite and kaolinite have essentially replaced them (Figure 3c). There are anhedral, interstitial quartz grains (25%–29% vol.%). Usually found as subhedral crystals, plagioclase ($An_{11–22}$) can also infrequently be found as laths (15%–22% vol.%). They have completely changed into saussurite. Subhedral fibers that are interstitial to quartz and plagioclase are primarily formed by sericitized muscovite (Figure 3c).

With a minor percentage of muscovite, syenogranites are hypidiomorphic, fine-to-medium-sized grains, and primarily composed of potassium feldspar, quartz, plagioclase, and biotite. The primary component that appears as a triple junction with undulose extinction is quartz (Figure 3d). Plagioclase is found as tabular crystals that range in shape from euhedral to subhedral and have distinctive lamellar twining (Figure 3e). Most of them are still fresh, but some are slightly saussuritized (Figure 3f). Although they make up only 1% of the rock, mafic minerals (biotite) are noticeable in some samples. The subhedral flakes that primary muscovite often develops are interstitial with quartz and plagioclase.

K-feldspar, plagioclase, and quartz constitute the majority of the medium-sized, hypidiomorphic grains of the Magal Gebreel alkali feldspar rocks, with trace amounts of muscovite and biotite crystals. K-feldspar (35–39 vol.%), the main constituent, is present in subhedral crystals as either string perthite or flamy perthite. They are occasionally mildly kaolinized and cracked. The crystallization of plagioclase ($An_{8–12}$) (18–22 vol.%) results in subhedral forms with albite twinning and zoning properties. Anhedral crystals of both primary and secondary generations of muscovite are found. Zoned zircon is found on the edges of quartz as a euhedral crystal (Figure 3g–i).

4.2. Mineral Chemistry

Some essential and accessory minerals (from MGGs) such as feldspars, mica, amphibole, zircon, columbite, thorite, monazite, xenotime, and wolframite were analyzed using electron microprobe analysis (EPMA).

Twenty spot-analyses of K-feldspars and nineteen plagioclase from MGGs were analyzed from granodiorite, monzogranites, syenogranites, and alkali feldspar rocks (Supplementary Table S1). The chemical composition of K-feldspars typically changes very little, with alkali feldspar rocks having low Na_2O, intermediate K_2O, and relatively high SiO_2. They exhibit a progressive increase in K_2O and decrease in Al_2O_3 from granodiorite to alkali feldspar granites. Notably, there is a progressive increase in orthoclase content, but albite decrease from granodiorite (av. $Or_{39.83}Ab_{6.28}$) towards alkali feldspar granites (av. $Or_{96}Ab_{3.8}$), and all of these types are of orthoclase composition [27] (Figure 4a). In contrast, younger rocks exhibit plagioclase's sodic albite composition, whereas granodiorite rocks (with mean end member $Or_{0.79}Ab_{85.65}An_{13.54}$) indicate oligoclase (Figure 4a). Among the investigated granites, granodiorite had the greatest CaO (av. 2.74 wt%) and anorthite content (av. 13.54 mol%).

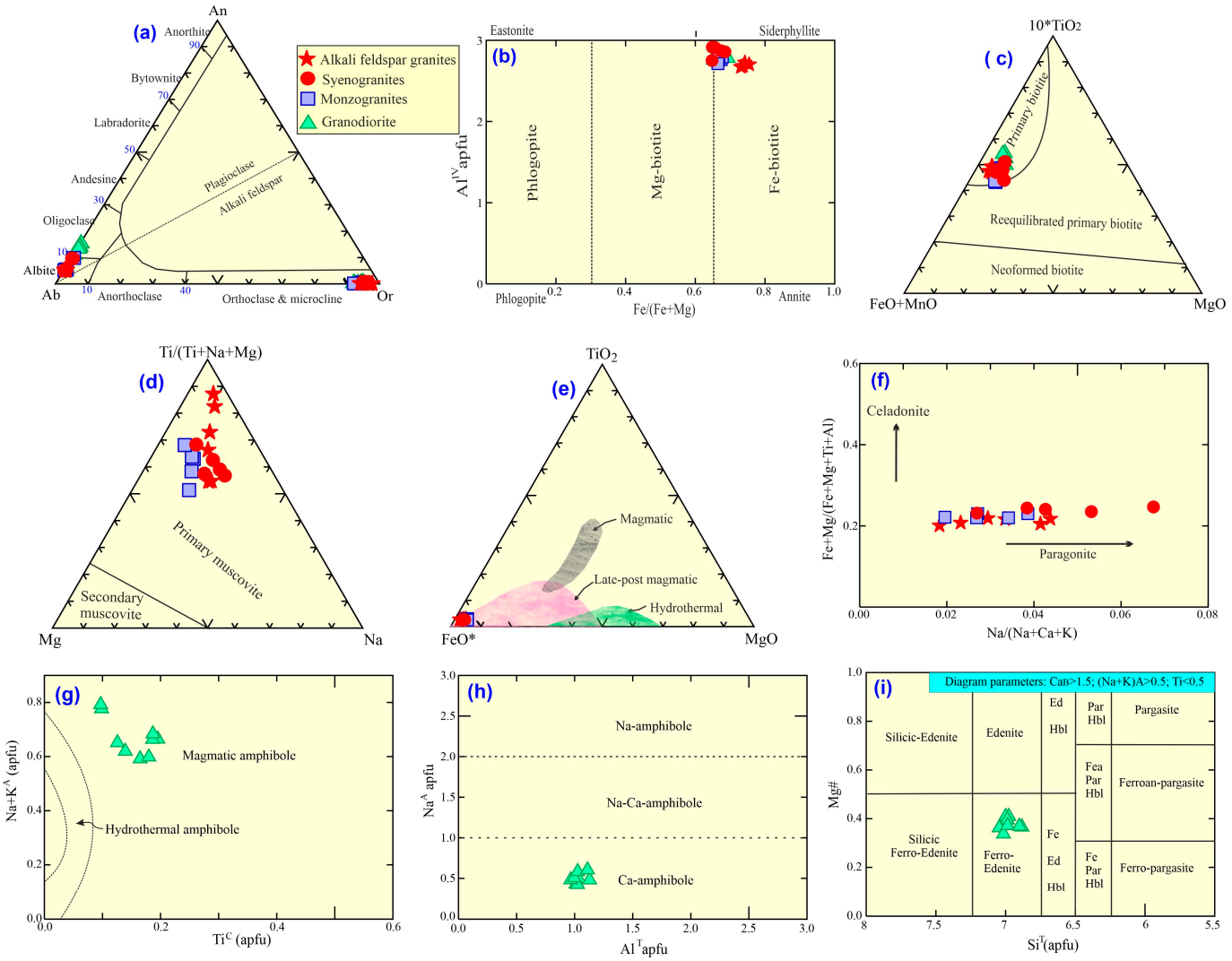

Figure 4. Mineralogy diagrams: (**a**) feldspar diagram [27]; (**b**) biotite diagram [27]; (**c**) ternary biotite diagram [28]; (**d**) ternary muscovite diagram [29]; (**e**) diagram of muscovite (FeO*-TiO_2-MgO) [30]. (**f**) Apfu ratios of muscovite cations [31]; (**g**) Ti^C- $(Na + K)^A$ diagram; (**h**) amphibole classification [32]; and (**i**) binary diagram (Si^T-Mg#) for amphiboles [32].

Supplementary Table S2 lists the results of the analysis of the trioctahedral (biotite) mica under examination. Granodiorite has the lowest average percentage of silica (av. 35.8%) and alumina (av. 17.53%) among the analyzed rocks; however, it has the highest FeO* (av. 25.54 wt.%), MgO (av. 7.34 wt.%), and TiO_2 (av. 3.62 wt.%) contents compared to other rocks from the studied post-collisional granites. The biotite compositions of the rocks under study are similar to one another and primarily composed of Fe-biotite [27] (Figure 4b). Furthermore, by utilizing the Fe# versus Al^{IV} diagram, the examined biotite demonstrates the siderophyllite composition. The chemistry of the investigated biotite and the primary biotite are consistent, based on the ternary diagram of Nachit [28] (Figure 4c).

The younger granites are the only ones that include the dioctahedral mineral muscovite (Supplementary Table S3). The chemical and textural constitution of muscovite is similar to that of muscovite of primary origin (Figure 4d) [29]. It contains TiO_2 (av. 0.32 wt.%), K_2O (av. 9.32 wt.%), MgO (av. 0.32 wt.%), and Na_2O (av. 0.22 wt.%). The low TiO_2 content supports a late/post-magmatic [30], (Figure 4e), while the increased Na_2O level in the muscovite under study indicates a paragonite component (Figure 4f).

The structural formulas of eleven amphibole spots, which are found solely in granodiorites, are listed in Supplementary Table S4. They have average compositions of SiO_2 (46 wt.%), FeO* (22.41 wt.%), MgO (7.72 wt.%), CaO (12.75 wt.%), and Al_2O_3 (6.34 wt.%). The binary diagram of Ti^C-Na + K^A (Figure 4g) shows that the Ti (apfu) content is above 0.096 and the $Na^A + K^A > 0.65$ is above 0.65, indicating primary origin [32,33]. The mean Al^T of ~1 indicates that the examined amphiboles are mainly calcic (Figure 4h). The categorized diagram indicates [32] (Figure 4i) that they are categorized as ferro-edenite. Moreover, the amphibole binary diagram [34] shows that they fall in the edenite field (Figure 5a).

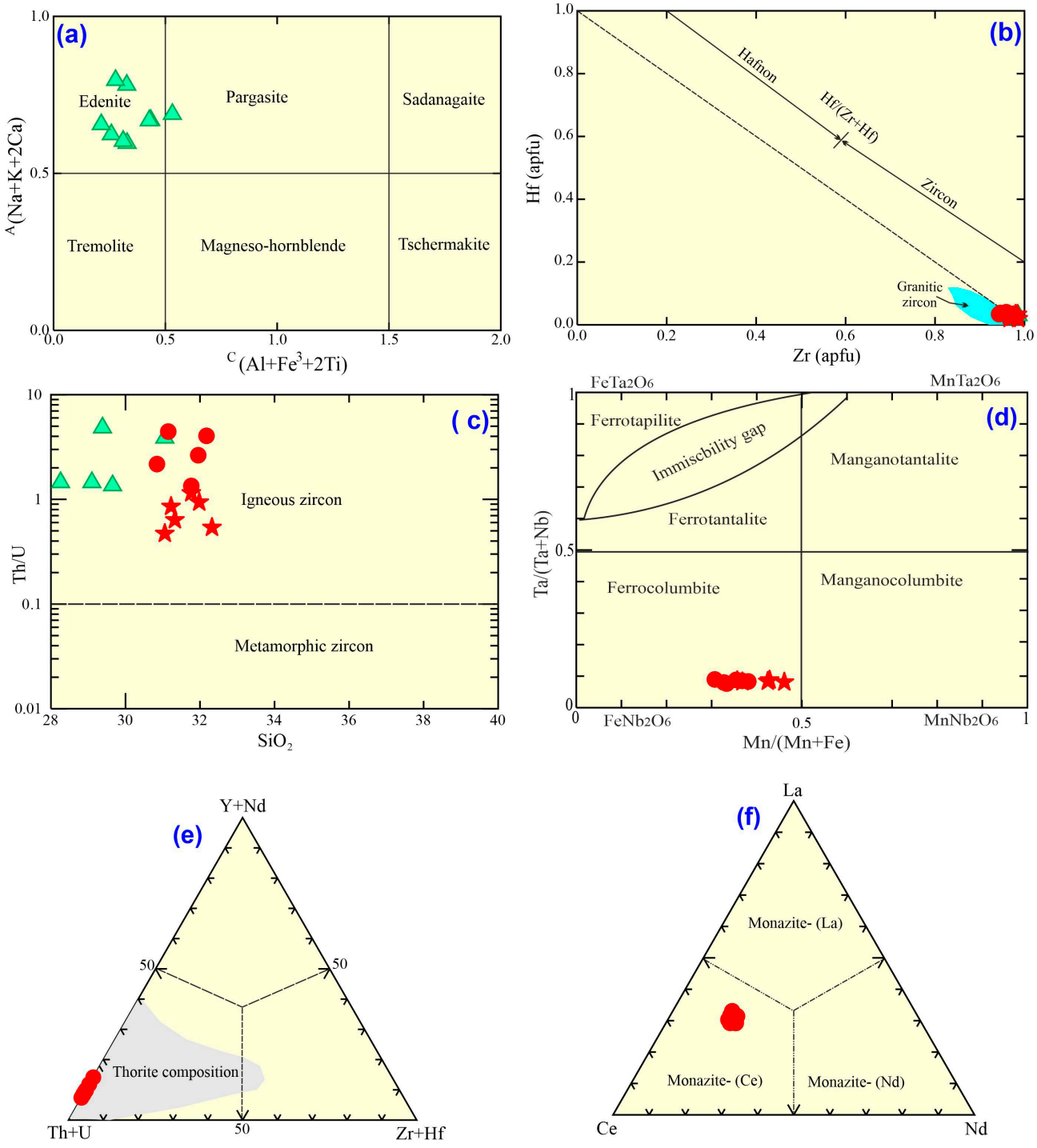

Figure 5. Mineralogy diagrams: (**a**) amphibole classification [34]; (**b**) binary Hf-Zr diagram; (**c**) zircon type discrimination [35]; (**d**) discrimination Nb#-Ta# diagram [36]; (**e**) thorite composition diagrams; (**f**) Ce-La-Nd contents for monazite. Symbols are as in Figure 4.

The most prominent accessory mineral found in the examined MGG rocks is zircon (Supplementary Table S5). Granodiorite has the highest ZrO_2 (av. 67.15 wt.%) content among the examined zircon, but the lowest SiO_2 (av. 28.78 wt.%) and HfO_2 (av. 3.1 wt.%) values. Furthermore, their chemical makeup closely resembles that of other oxides. The mean zircon under examination has a high Zr/Hf = 31.73 ratio, which is in harmony with granitic rock zircons (Figure 5b). The studied zircon has a mean Th/U ratio of 2.66, as is common with igneous zircon, and is primarily found in the magmatic field [35] (Figure 5c).

Nb-Ta minerals are examined and mentioned in Supplementary Table S6, and frequently occur in extremely fractionated magma. High levels of Nb_2O_5 (avg. 63.65 wt.%), Ta_2O_5 (avg. 10.98 wt%), FeO* (av. 10.13 wt%), and significant amounts of MgO (av. 7.91 wt%) and MnO (av. 5.39 wt%) were found in the columbite from both alkali feldspar and syenogranites under study. The Mn#-Ta# classification diagram [36] (Figure 5d) indicates that they are ferro-columbite.

The EPMA that was conducted for thorite is mentioned in Supplementary Table S7. ThO_2 (av. 70.6 wt.%) is notably high in the analyzed thorite, and Y_2O_3 (av. 4.05 wt.%), CaO (av. 1.6 wt.%), and FeO* (av. 2.2 wt.%) are also present in significant amounts (Figure 5e).

In addition to significant amounts of traces like ThO_2 (5.94–10.69 wt.%), the monazite analysis shows that they have enrichment of REE oxides such as Ce_2O_3 (27.03–29.47 wt.%), Nd_2O_3 (9.36–10.78 wt.%), La_2O_3 (15.22–18.14 wt.%), Pr_2O_3 (3.12–3.89 wt.%), and Sm_2O_3 (0.52–0.79 wt.%) (Supplementary Table S8). Monazite is classified as Ce-monazite (Figure 5f), and its composition is comparable to those of Mahdy [37].

Similarly, only syenogranites record xenotime. With significant amounts of HREEs like Gd_2O_3 (av. 3.25 wt.%), Dy_2O_3 (av. 4.45 wt.%), Er_2O_3 (av. 4 wt.%), Yb_2O_3 (av. 4.39 wt.%), and Sm_2O_3 (av. 46.47 wt.%), as well as the absence of LREEs (Supplementary Table S9), it exhibits a notable enrichment of P_2O_5 (av. 36.57 wt.%) and Y_2O_3 (av. 46.47 wt.%). Furthermore, wolframite is only found in syenogranites. It is mainly composed of MnO (av. 18.64 wt.%), FeO* (av. 4.33 wt.%), and WO_3 (av. 76.74 wt.%) (Supplementary Table S10).

4.3. Whole-Rock Geochemistry

4.3.1. Classification

We can categorize and verify the names, tectonic setting, and chemical affinities of each species of the studied rocks utilizing bulk-rock compositions. The whole rock chemistry of twenty-three samples from the MGGs (five granodiorite, five monzogranites, five syenogranites, and eight alkali feldspar granites) is shown in Supplementary Table S11. Different types of granitic rocks can be categorized using different classification diagrams. The analyzed MGGs rocks fall into the granite and granodiorite field, as revealed in the Middlemost [38] total alkali silica (TAS) for the granite classification diagram in Figure 6a. Furthermore, the MGGs samples straddle the granodiorite, monzogranites, syenogranite, and alkali feldspar domains according to the Q-ANOR normative diagram [39] (Figure 6b).

4.3.2. Compositional Variations

In comparison to other MGGs, the alkali feldspar rocks have the highest total alkalis (av. 8.78 weight percent), the lowest Fe_2O_3 + MgO concentration (av. 0.52), the highest SiO_2 (av. 75.3 weight percent), the lowest Fe_2O_3/MgO ratio (av. 26.31), and the highest Fe# (av. 0.96). This implies that instead of being magnesian (granodiorite) [40], these rocks are ferroan (also monzogranites and syenogranites). The granodiorite samples contain the highest plagioclase (Ab + An) content of 45.19, according to the computed normative composition, which is supported by the high quantities of Sr (av. 276.6 ppm) and Ba (av. 509 ppm). On the other hand, the alkali feldspar rocks include minimal amounts of

Fe_2O_3 (av. 0.49 weight percent), TiO_2 (av. 0.02 wt.%), MgO (av. 0.02 wt.%), and CaO (av. 0.34 wt.%), but significant amounts of SiO_2 (av. 75.31 wt.%) and K_2O + Na_2O (av. 8.78 wt.%).

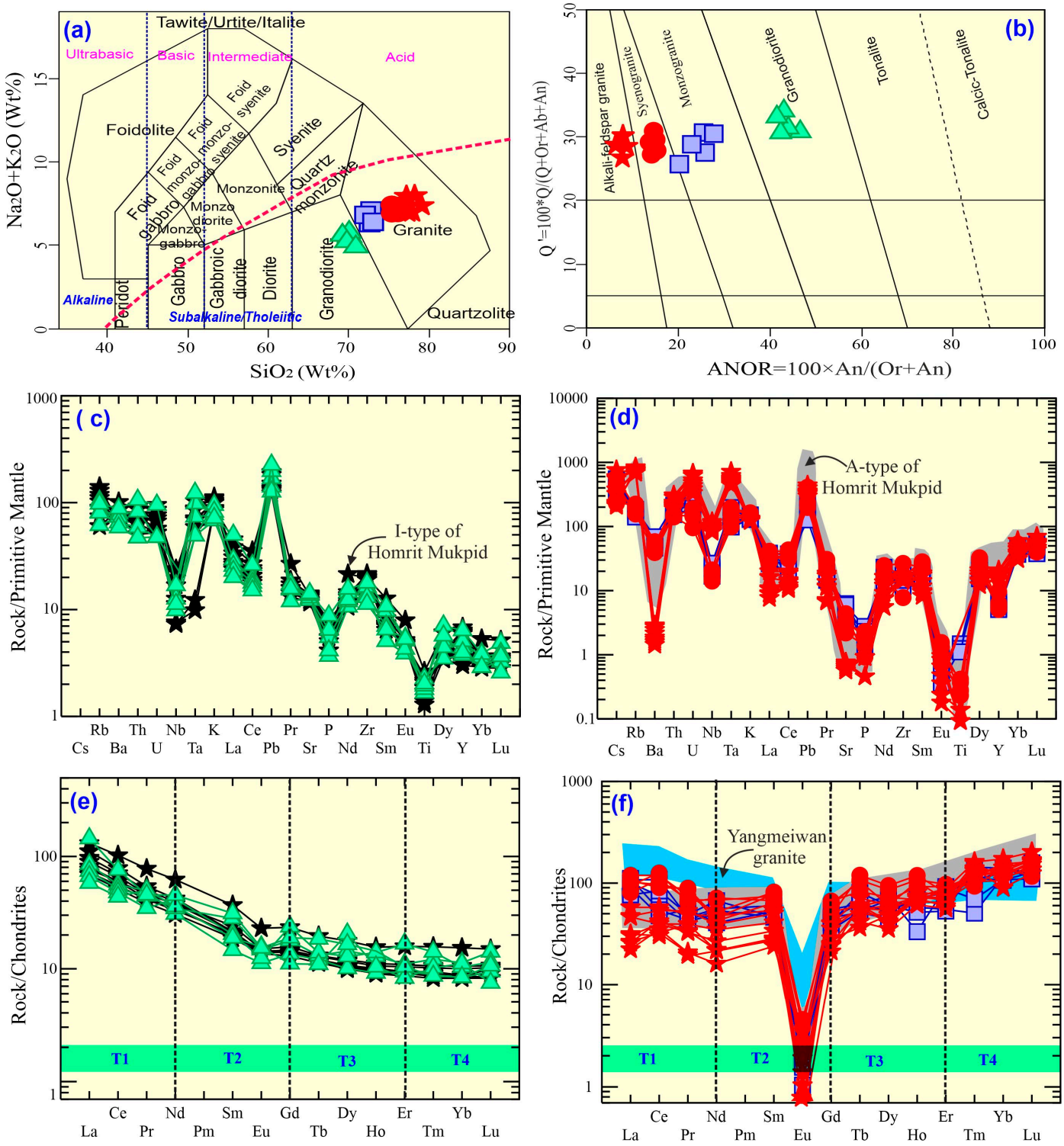

Figure 6. Bulk-rock diagrams: (**a**) binary diagram of Middlemost [38]; (**b**) Q′-ANOR normative diagram [39]; (**c**) trace elements of granodiorite contrast with those of Sun and McDonough [41]; (**d**) trace elements of younger granites contrast with those of Sun and McDonough [41]; and (**e**,**f**) REEs contrast with chondrite [41] for granodiorite and younger granites, respectively. I- and A-types of the Eastern Desert (Homrit Mukpid) [20] and A-type of Yangmeiwan granite [42] are used for comparison. Symbols are as in Figure 4.

To show the relationship between the SiO_2 content and some chosen elements of the MGGs, Harker variation diagrams were drawn. Granodiorites exhibit lower abundances of $Fe_2O + K_2O$, $Fe_2O_3^*/Fe_2O_3^* + MgO$, Ta, Rb, and Y than other younger granites, but greater concentrations of $Fe_2O_3^*$, CaO, TiO_2, P_2O_5, MgO, Ba, Sr, and V (Figure 7). Figure 7 shows that the major and trace elements have obvious linear positive and negative interactions with SiO_2. In the examined MGGs, the alkali feldspar rocks exhibit low levels of Ba and V and high quantities of Rb, Nb, Sn, Ga, Ta, Th, Y, and U.

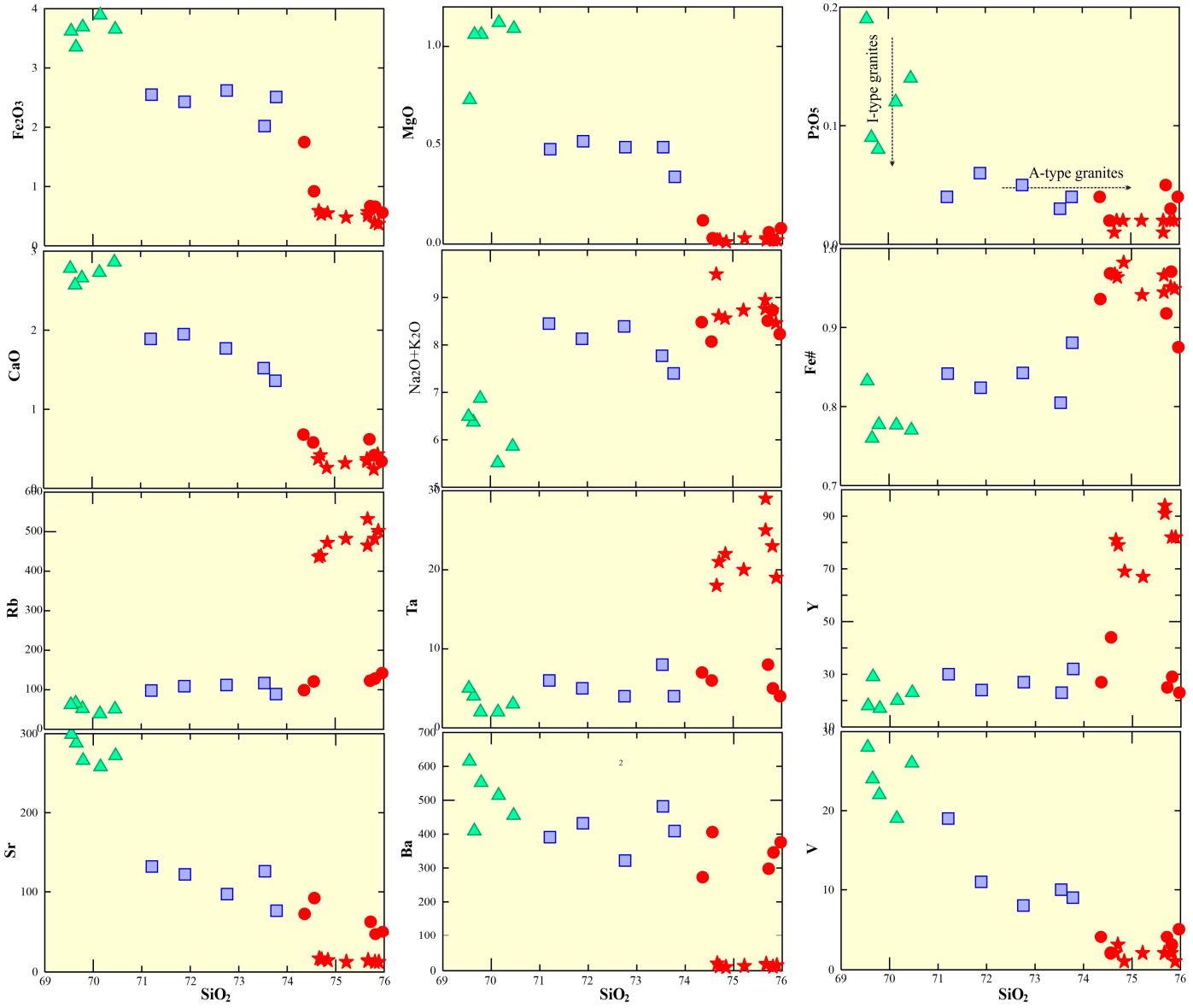

Figure 7. Harker's binary diagrams between SiO_2 and others (major, trace, and ratios). Symbols are as in Figure 4.

Granodiorite exhibits strong positive lead anomaly, and considerable negative P, Nb, and Ti anomalies (Figure 6c) [41]. A noticeable elevation of LILEs (Ba, K, and Rb) compared to HFSEs (Zr, and Nb), which are consistent with those of the Eastern Desert's I-type granites [20]. The syn-tectonic setting is demonstrated by these studies. Conversely, the younger granites (alkali feldspar granites, monzogranites, and syenogranites) exhibit negative Ti, Ba, P, Nb, and Sr anomalies that are consistent with those of A-type from the Eastern Desert [20] and A-type of Yangmeiwan granite [42]. The extreme fractionation of ilmenite, apatite, and plagioclase is responsible for this (Figure 6d).

Supplementary Table S11 lists the REE concentrations in the rocks that are being studied. There is no doubt that the MGGs have different patterns of REEs. Granodiorite exhibits a significant LREE (av. 79.22 ppm) to HREE (av. 14 ppm) enrichment (Figure 6e), which is comparable with that of I-type from the Eastern Desert granites [20]. They have mean ∑REEs (av. 93.2) that are lower than the Hermann [43] global average. From the other side, the younger granite patterns under study exhibit a very noticeable negative anomaly in Eu (Figure 6f) and a small elevation in LREEs in relation to HREEs (except for alkali feldspar samples; Supplementary Table S11). These anomalies are consistent with Sr and Ba abnormalities, which are most likely related to fractionated plagioclase and K-feldspar abundance.

5. Discussion

5.1. Lanthanide Tetrads

In particular, the Irber [44] technique is frequently employed to evaluate the tetrad effect of REEs (fourteen lanthanide elements). Kawabe [45] (Figure 6f) classified lanthanides into four groups (T1, T2, T3, and T4); because Pm is usually absent and Eu behaves negatively, it is challenging to identify the second tetrad [46]. The REEs patterns can be either convex or concave [47].

The mean values of the examined granodiorite (av. 0.89) and monzogranites (av. 0.81) are less than 1.1, indicating that they do not exhibit the convex tetrad type effect in T1 ($Ce/Ce^* \times Pr/Pr^* = T1$). With mean values of 1.22 and 1.24, respectively, the syenogranites and alkali feldspar rocks in T1 display a convex tetrad-type effect (Figure 6f). However, no concave tetrad-type effect was observed in the rocks under examination, with T3 ($Tb/Tb^* \times Dy/Dy^* = T3$) values less than 0.9. The mean tetrad intensities ($TE_{1,3}$) vary from 0.89 (granodiorite) to 1.19 (syenogranites).

According to Jahn [48], the chondritic values of the La/Nb and La/Ta ratios are 0.96–1 and 16–18, respectively. According to Irber [44], the La/Nb ratios of the examined samples are not in the range of chondritic value, suggesting a non-CHARC nature. This points to fluid-rich processes.

5.2. Thermobarometry Crystallization Conditions

Temperatures, depths, and pressures can be determined for the investigated felsic plutonic rocks using bulk chemistry and mineral chemistry data in order to understand their evolution. Basak and Goswami [49] assert that there is no question that the distinctive features of the magma and mineral assemblages are intimately linked throughout the stages of crystallization. Temperatures based on zircon saturation (T_{Zr}) were computed using the Watson and Harrison [50] equation, which relies on the presence of zircon in the bulk rock chemistry of the granites studied. For the MGG granodiorite, monzogranites, syenogranites, and alkali feldspar rocks, the average temperature at which they originated was 740, 723, 769, and 762 °C, respectively. Normally, syenogranites and alkali feldspar rocks have a crystalized temperatures between 750 and 830 °C, which are in accord with ANS A-type granites [51]. The granitic rocks under investigation have increased T_{Zr}, which indicates that the magma source was extremely hot, facilitating zircon saturation. Using the chemical analysis of plagioclase, the crystallization temperature of the MGGs under study was established [52]. When the examined plagioclase is placed on the An-Ab-Or diagram (Figure 8a), a predicted plagioclase temperature of the Magal Gebreel granodiorite is around 840 °C, which exceeds the predicted temperature for younger granites (810–840 °C).

According to Henry [53], the Ti content of biotite is a very sensitive marker for the temperature at which biotite crystallization occurs. It is possible to obtain the temperatures

by employing the Ti (0.22–0.44) and Mg# (0.25–0.35) contents of biotite. The Henry [53] binary of Ti against Mg/(Mg + Fe) plot (Figure 8b) yielded biotite temperatures varying from 690 °C to 710 °C for granodiorite and between 550 and 650 °C for the younger granites. Furthermore, according to Uchida [54], the total Al content (Al^T) of biotite is susceptible to pressure and rises with crystallization pressure. Accordingly, the Al^T concentration of biotite is suitable for usage to determine the solidification pressure (P) and/or the magma depth using the following formula: P (kbar) = 3.03 × Al^T − 6.86 [54].

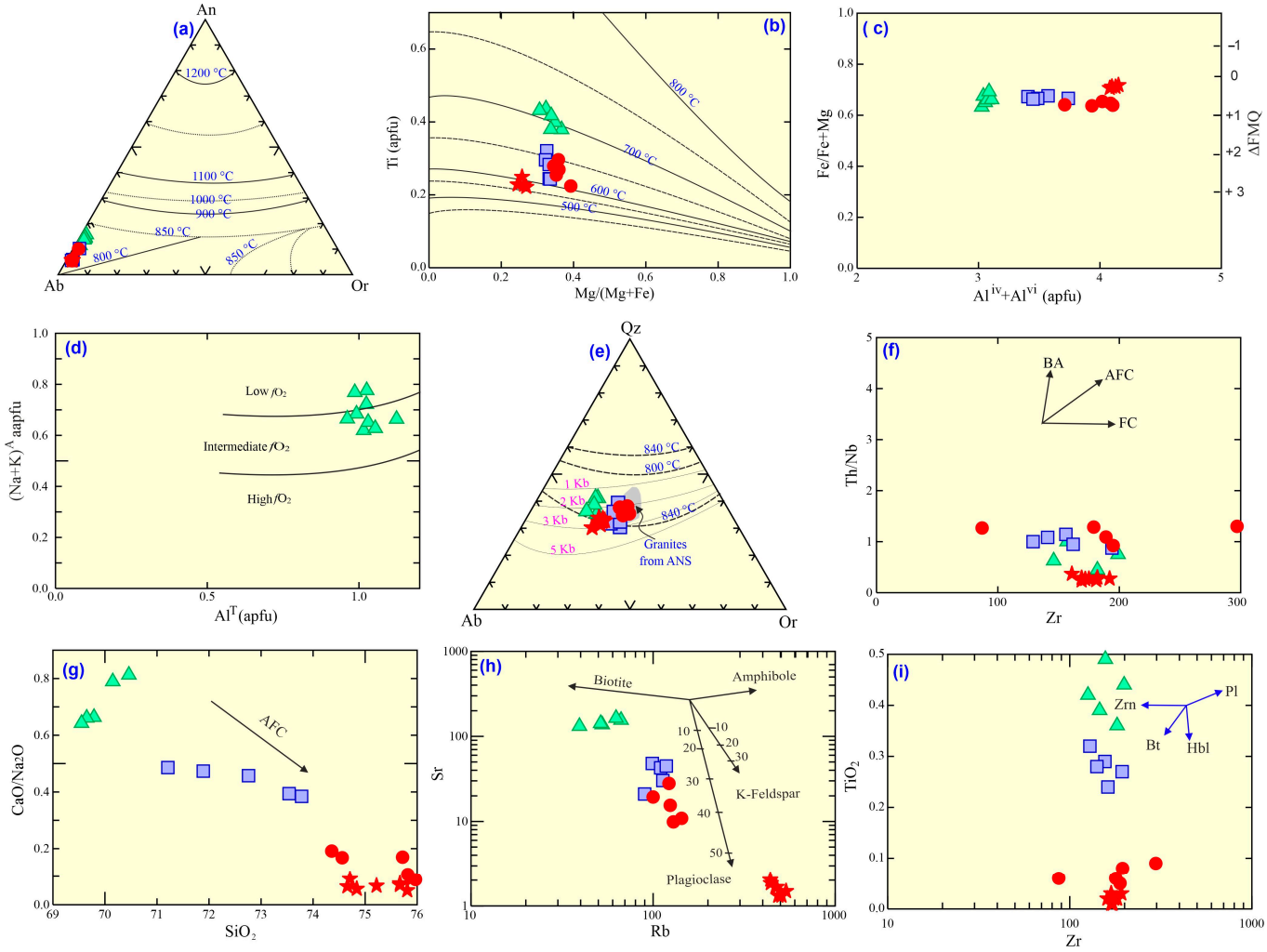

Figure 8. (**a**) Plagioclase thermometry [52]; (**b**) biotite Mg# vs. Ti diagram [53]; (**c**) Fe# vs. Al^T diagram [55]; (**d**) amphibole crystallization [56]; (**e**) thermobarometry utilizing bulk rock analysis [57]; (**f**) Th/Nb-Zr diagram [58]; (**g**) SiO_2 via CaO/Na_2O diagram; (**h**) Rb vs. Sr diagram; and (**i**) Zr vs. TiO_2. Symbols are as in Figure 4.

By using this experimental equation, the average pressures for granodiorite, monzogranites, syenogranites, and alkali feldspar rocks are 2.43, 3.84, 5.14, and 5.68 kbar, respectively. Furthermore, oxygen fugacity (fO_2) can be calculated with the use of the biotite chemistry. According to Anderson [55], the examined MGGs have a restricted range of Fe/(Fe + Mg) ratios (0.6–0.75), showing that they crystallized between ~QFM +0.1 and QFM +1 under moderately oxidizing circumstances (Figure 8c). Oxygen fugacity (fO_2) can be detected petrogenetically using amphibole chemistry. The low-to-intermediate fO_2 field is where the examined granodiorite samples plot (Figure 8d). The ANS granites (Figure 8e) are consistent with the normative values of the primary analysis of MGGs, which reflect

that the rocks under study were derived from crustal substances at pressures of 1–3 kbar and temperatures ranging from 820–850 °C [57].

5.3. Fractionation and Crustal Contamination

The studied granitic rocks consider a range of compositional changes in their parent melts, involving fractionation and crustal contamination. Magmatic processes such as assimilation-fractional crystallization (AFC), bulk assimilation (BA), and fractional crystallization (FC) can be inferred using some ratios [59]. Significant magmatic separation from the original melts is indicated by the consistently high ratios of FeO/MgO in the examined granodiorite (av. 3.68), monzogranites (av. 5.37), syenogranites (av. 19.28), and alkali feldspar (av. 26.31). The binary Th/Nb ratio vs. Zr plot of the granitic rocks under investigation shows a distinct FC trend (Figure 8f).

Additionally, as the SiO_2 content increases, the CaO/Na_2O ratio decreases from granodiorite (av. 0.44) to alkali feldspar (av. 0.07) (Figure 8g). The examined granitic rocks show an AFC trend through this CaO/Na_2O connection via SiO_2. Additionally, the Rb vs. Sr plot (Figure 8h) shows feldspar fractionation preferences in younger granites, which reflect the primary component in these rocks in varying proportions. Plagioclase fractionation is observed in the distinct systematic variation of Rb, Sr, and Ba from granodiorite to alkali feldspar rocks (Figure 7), which is in accord with those of El-Awady and Lasheen [19,20]. Furthermore, the adverse relations of P_2O_5, TiO_2, Fe_2O_3, and V via SiO_2, as well as the negative anomalies of Ti, Ba, Sr, and P in the trace patterns (Figure 6d), may be ascribed to fractionation of plagioclase, apatite, and ilmenite minerals. The SiO_2-Rb positive association in alkali feldspar rocks undoubtedly indicates K-feldspar accumulation for the post-collisional granites. Additionally, amphibole fractionation throughout evolution may be shown by the decrease of TiO_2, CaO, Fe_2O_3, MgO, and via SiO_2 (Figures 7 and 8i).

The ferromagnesian silicates may be the cause of the linear decrease of Fe_2O_3 and MgO with increasing SiO_2. Granodiorites, one of the rocks under examination, have a comparatively low SiO_2 content (av. 70 wt.%) and exhibit magnesian character [40] (Figure 9a), supporting the idea that basaltic melt contaminated them. Furthermore, the granodiorites have a slight Eu negative anomaly, which suggests a minimal impact of plagioclase fractionation, but the noticeable negative Eu anomaly in the younger granites under examination may imply heavy plagioclase fractionation from their parent melt. The examined MGGs exhibit a markedly broad mean ∑REE content as well as LREE enrichment in comparison to HREEs (except for alkali feldspar rocks) (Figure 6f), indicating the fractionation role during evolution. The Ba/Nb ratio varies greatly between the syn- and post-collision kinds of MGGs, ranging from granodiorites (av. 60.5) to alkali feldspar samples (av. 0.21). Furthermore, the Zr/Nb ratios of alkali feldspar samples (av. 0.21) and granodiorites (av. 19) differ significantly, which further supports the impact of continental crustal contamination.

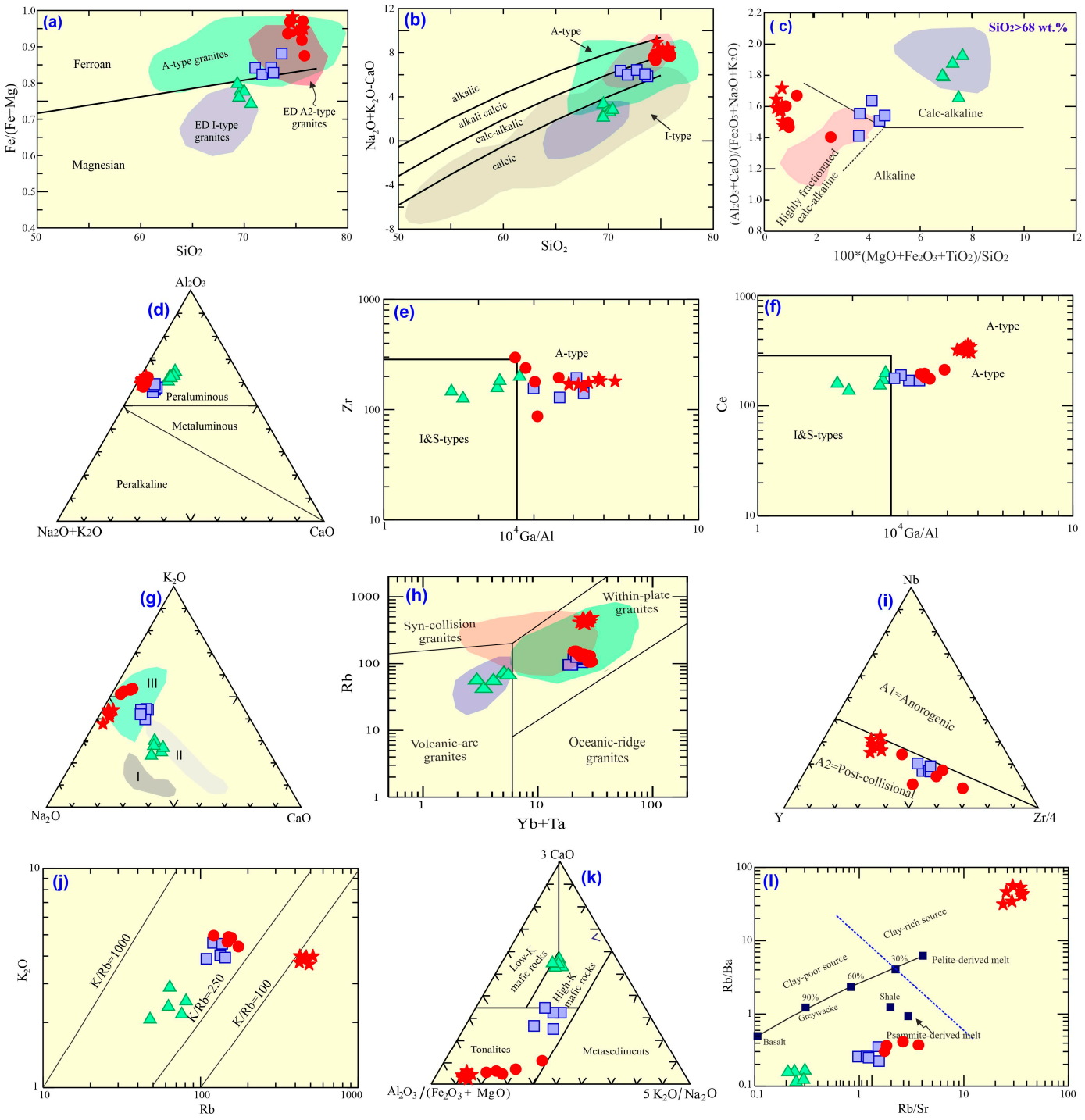

Figure 9. (**a**) Fe#-SiO_2 [40], fields of A2- and I-types of the Eastern Desert (ED) granites [18]; (**b**) SiO_2-K_2O + Na_2O-CaO [40]; (**c**) diagram of major oxides [60]; (**d**) ternary diagram of aluminous affinity [61]; (**e**,**f**) genetic type of granitic rocks [21]; (**g**) CaO-K_2O-Na_2O diagram [62]; (**h**) tectonic Rb-Yb + Ta diagram [63]; (**i**) Y-Nb-Zr/4 ternary diagram [64,65]; (**j**) K-Rb diagram [66]; (**k**) experimental diagrams [67,68]; and (**l**) Rb/Ba-Rb/Sr [69]. Symbols are as in Figure 4.

5.4. Magma Affinity and Tectonic Setting

One primary purpose of bulk-rock analysis of the rocks under study is to clearly identify the kind of magma and petrogenetic linkages. According to Middlemost [38], the examined rocks are subalkaline (Figure 6a). While younger granites plot in A-type granites and are in concord with the Eastern Desert's A2-type granites [18], the calcic granodiorite is in concord with the Eastern Desert's I-type granites [18,20] (Figure 9b).

They have agpaitic (AI) ratios of av. 0.81, 0.82, and 0.85 for monzogranites, syenogranites, and alkali feldspar, respectively. With an AI of less than 0.6, granodiorite is calc-alkaline. Plus, the younger granites under study lie within the highly fractionated magma field (Figure 9c) [60]. They are peraluminous rocks [61] (Figure 9d). Mg#, CaO, P_2O_5, MgO, Fe_2O_3, Sr, and Ti are depleted in the MGGs younger granites, while SiO_2, Fe_2O_3/MgO, Nb, Zr, Ce, Zn, and Ga/Al are quite abundant. Numerous figures, such as those produced by Frost [70] (Figure 9a,b), Whalen [21] (Figure 9e,f), and Li [71] (Figure 7), can be used to differentiate and illustrate the A-type feature of the MGGs younger granites.

Furthermore, these rocks are definitely syenogranites and alkali feldspar rocks, which exhibit an A-type character due to their Rb/Sr ratio exceeding unity [72]. Furthermore, it is clear that the trace (Figure 6c,d) and REE (Figure 6e,f) patterns of the younger granites of MGGs have distinct character and are clearly compatible with those of the younger granites that were formed during post-collision [20]. The ternary categorized diagram of Hassan and Hashad [62] shows that the granodiorite plot is in the early phase of subduction granites (II) field, while the younger granites of the MGG are located inside the field of the later subphase (III) (Figure 9g) of younger granites. Granodiorite plots in the arc field and is in accord with Eastern Desert I-granites [18,20], according to the Y + Ta vs. Rb diagram [63], while the younger granites under examination overlap within plate, A-type granites, and Eastern Desert A2-granites [18,20] (Figure 9h).

A1 (within plate/rifting) and A2 (post-collision) are possibly identified because to the younger granite rocks located in A2 that make up the studied MGGs [64,65] (Figure 9i). In contrast, the Rb/Sr ratio of Magal Gebreel granodiorite is significantly lower relative to younger granites, ranging from 0.15 to 0.23, indicating I-type granites, as shown by many diagrams (Figures 7 and 9). Amphiboles and biotite predominate as mafic silicates (Figure 3a,b), and the frequent presence of sphene and iron oxides as accessory phases indicate the I-type geochemical nature of the granodiorite under study. The compositions of the examined granodiorites are similar to those of Eastern Desert's I-type granites in terms of major oxide, trace (Figure 6c,d), and rare-earth elements (Figure 6e,f).

5.5. Petrogenesis and Source of Magal Gebreel Felsic Plutonic Rocks

The Egyptian Eastern Desert's granitic rocks might have been developed via the syn-, late-, and post-collision of East and West Gondwana [5,20]. They are diverse in depth and time of formation, as evidenced by their variances in their mineralogy, age, chemistry, and color [2,40]. The crustal rocks may contaminate these mantle magmas if they rise to a shallow depth [73]. The MGGs are thought to have been created by fractionation and melting stages, as stated by Cao et al. [74]. The reduction in amounts of Ti, Sr, and Ba, along with positive anomalies for Rb and Pb (Figure 6c), demonstrate the fractional crystallization process, indicating strong Ti-rich and plagioclase fractionation.

The petrogenesis of the studied MGGs can be deduced from specific ratios, like Rb/Sr, Rb/Ba, Sr/Ba, and Rb/Zr. The Rb/Sr values of the rocks under study (av. 0.2, 0.98, 2.07, and 35.82 for granodiorite, monzogranites, syenogranites, and alkali feldspar, respectively) are greater than the values of the mantle source (Rb/Sr $\leq$ 0.1), indicating that the rocks are coming from crustal materials, according to Taylor and McLennan [75]. They have a regular crustal origin, as indicated by their low Rb/Ba, Rb/Zr, and Sr/Ba ratios (Supplementary Table S11). The analyzed rock patterns (Figure 6c,d) exhibit a negative Nb anomaly, pointing to the involvement of a crustal origin [58]. The rocks under investigation are situated between a mantle-derived magma (K/Rb = 1000) [66] and a standard crustal source (K/Rb = 250) (alkali feldspar plot at K/Rb = 100) (Figure 9j), suggesting that they emanate from crustal sources [76].

Different melting degrees of mafic rocks [77,78], fractionation of mafic mantle magma [79], and felsic and mafic mingling [20,76,80] are some of the possible causes of the formation of the calc-alkaline and I-type granites. A subduction-related origin is suggested by the geochemical fingerprint of the granodiorite under investigation, which includes LREEs elevation in relation to HREEs, considerable LILEs enrichment, and noticeable negative Ti, P, and Nb anomalies. The granodiorite may have formed from the melting of high-K basaltic rocks, which are located near basalt and clay-poor sources, according to source experimental diagrams [67,68] (Figure 9k,l).

The MGG younger rocks have high Rb/Nb ratio (7.96, 9.82, and 7 for alkali feldspar, syenogranites, and monzogranites, respectively), indicating a crustal tonalitic source [81]. However, the peraluminous character suggests melting of the metasediments, as supported by low average Fe_2O_3 + MgO composition of the studied rocks (0.52, 0.97, and 2.89 wt.% for alkali feldspar, syenogranites, and monzogranites, respectively) [82]. Additional details include the observed MGGs having a notably high Al_2O_3/TiO_2 ratio for monzogranites (av. 48.4), syenogranites (av. 211), and alkali feldspar (av. 837.4), which reflect limited partial melting of metasediments [69,83]. Additionally, the elevation of Rb in syenogranites (av. 123 ppm) and alkali feldspar (av. 476 ppm) relative to Sr (av. 13.5 and 64.2 ppm, respectively), high K_2O, and low CaO contents suggests a pelitic parent source [84]. In the Rb/Sr vs. Rb/Ba relationships, the younger granites of the MGG are of clay-poor (monzogranites and syenogranites)/rich (alkali feldspar rocks) origin [69], as seen in Figure 9l.

5.6. Geodynamic Modelling

The main Eastern Desert crystalline rocks of the ANS are generally composed of granitic rocks [7]. Diverse tectonic regimes are reflected in their variations in color, texture, and magma chemistry. We can conclude from the explanation above that the MGGs under investigation were generated in two distinct stages as they moved from the subduction (635–620 Ma) to the post-collisional stage (600 ± 10 Ma) [2,85]. The transition took place at 600 ± 10 Ma, which was accompanied by the post-collisional granitic intrusion. The occurrence of I-type granodiorites, throughout the accumulation of arcs onto the East Gondwana edge during the formation of the ANS crust, marked the initial phase of the MGGs (Figure 10a). The decomposition of a subducting slab produced granodiorites, which facilitated in the creation of high-K mafic magmas and mantle melting. These magmas then penetrated the continental crust and formed the calc-alkaline granodiorites through fractional crystallization (Figure 10a). In contrast, the current study revealed that the younger granites of MGGs originated at the extensional stage, or late-to-post-collision (600 ± 10 Ma), at the culmination of the juvenile ANS maturation. Support to the thickening of the lithospheric layer may result in the high melting required for this occurrence (Figure 10b). A thick layer in the site of collision led to thermal and gravitational instability. This caused the slab to break apart (lithosphere delamination), which caused crustal doming, asthenosphere elevation, and underplating mafic magma [1,86]. The upwelling of asthenospheric melts resulted in richness in HFSEs such as Nb, Ta, Zr, Sn, and others. This magma penetrated into the lower crust via large faults and regions of shear. These faults and shear zones provided a suitable route for elevating fluids, volatiles, and melts originating from the mantle.

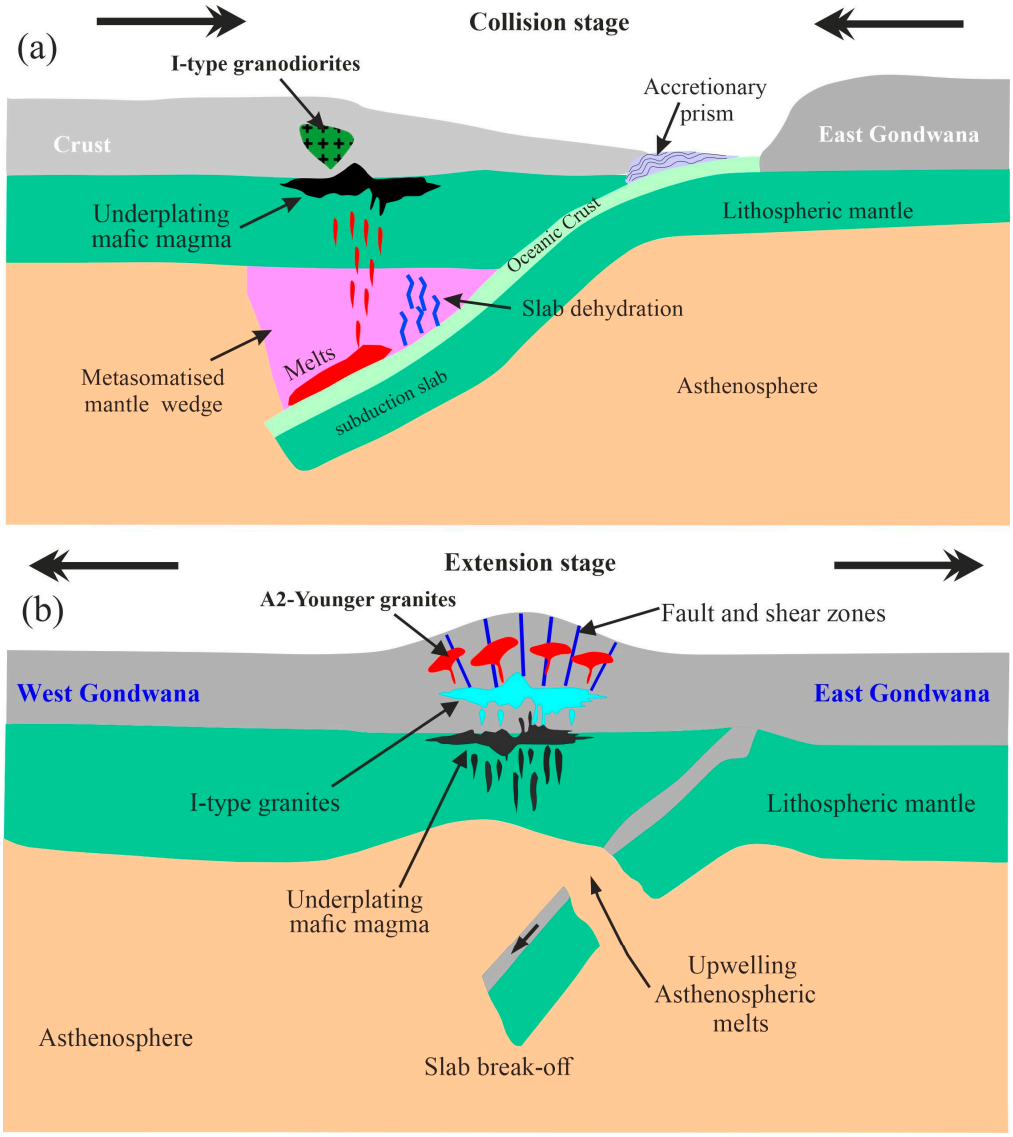

Figure 10. Evolution sketch of the two granitic Magal Gebreel phases: (**a**) subducted-related granodiorite; and (**b**) A2 younger granites [19,20].

6. Conclusions

From a combination of the field observation, petrography, mineralogical, and geochemical composition, we can conclude the following;

- Magal Gebreel felsic magmatism comprise I-type (granodiorites) and A2-type (monzogranites, syenogranites, and alkali feldspar rocks).
- Granodiorites exhibit negative Ti, P, and Nb anomalies in their patterns and they are calcic, calc-alkaline, and magnesian. They are frequently developed by melting of high K-basaltic sources, exhibit a clear enrichment of LILEs in comparison to HFSEs, and are comparable with the volcanic arc granites.
- The A2-type of MGGs have low contents of Mg#, P_2O_5, MgO, Fe_2O_3, Sr, and Ti, and have large quantities of SiO_2, Fe_2O_3/MgO, Nb, Zr, and Ga/Al. Additionally, they show a considerably negative anomaly in Eu and a slight elevation in LREEs compared to HREEs.
- The average temperature at which the Magal Gebreel rocks originated was 740, 723, 769, and 762 °C for granodiorite, monzogranites, syenogranites, and alkali feldspar rocks, respectively, according to the zircon saturation temperature (T_{Zr}). The rocks

under examination originated from crustal components at a pressure of less than 3 kbar and a temperature ranging from 820 to 850 °C in the upper continental crust, according to the normative values of Magal Gebreel rocks.

Supplementary Materials: The following supporting information can be downloaded at: https://www.mdpi.com/article/10.3390/min15070751/s1. Table S1: Representative electron microprobe analyses of feldspar minerals of the Magal Gebreel rocks. Table S2: Representative electron microprobe analyses of biotite of the Magal Gebreel rocks. Table S3: Representative electron microprobe analyses of muscovite of the Magal Gebreel rocks. Table S4: Representative electron microprobe analyses of amphibole of the Magal Gebreel rocks. Table S5: Representative electron microprobe analyses of zircon of the Magal Gebreel rocks. Table S6: Representative electron microprobe analyses of Nb-Ta minerals of the Magal Gebreel rocks. Table S7: Representative electron microprobe analyses of thorite minerals of the Magal Gebreel rocks. Table S8: Representative electron microprobe analyses of monazite mineral of the Magal Gebreel rocks. Table S9: Representative electron microprobe analyses of xenotime mineral of the Magal Gebreel rocks. Table S10: Representative electron microprobe analyses of wolframite mineral of the Magal Gebreel rocks. Table S11: Bulk rock analysis of the Magal Gebreel rocks.

Author Contributions: Conceptualization, E.S.R.L., G.M.S.; data curation, E.S.R.L.; funding acquisition F.A., I.V.S.; investigation, E.S.R.L., M.S., G.M.S.; methodology, G.M.S.; project administration, M.S., A.E.-T., E.S.R.L.; software, E.S.R.L.; supervision, E.S.R.L., F.M.K., M.S., I.V.S.; validation, E.S.R.L., M.S., I.V.S.; visualization, E.S.R.L., G.M.S., F.M.K.; writing—original draft, E.S.R.L.; writing—review and editing, E.S.R.L., G.M.S., A.E.-T., F.A., M.S., I.V.S., F.M.K. All authors have read and agreed to the published version of the manuscript.

Funding: This research received no external funding.

Data Availability Statement: All results are present within the text of the manuscript.

Acknowledgments: The authors extend their appreciation to the King Saud University for funding through the ongoing research funding program (ORF-2025-1120), King Saud University, Riyadh, Saudi Arabia.

Conflicts of Interest: There is no conflict of interest.

References

1. Fowler, A.-R.; Hamimi, Z. Lithospheric Delamination in Models of Post-Collision Tectonics in the Egyptian Eastern Desert and Sinai: Claims versus Evidence. *J. Afr. Earth Sci.* **2023**, *203*, 104948. [CrossRef]
2. Johnson, P.R.; Andresen, A.; Collins, A.S.; Fowler, A.R.; Fritz, H.; Ghebreab, W.; Kusky, T.; Stern, R.J. Late Cryogenian–Ediacaran History of the Arabian–Nubian Shield: A Review of Depositional, Plutonic, Structural, and Tectonic Events in the Closing Stages of the Northern East African Orogen. *J. Afr. Earth Sci.* **2011**, *61*, 167–232. [CrossRef]
3. Saleh, G.M.; Kamh, S.Z.; Abdalla, F.; Kilias, A.; Lasheen, E.S.R. A New Occurrence of Rift-Related Damtjernite (Ultramafic) Lamprophyre, Gebel Anweiyib Area, Arabian Nubian Shield: Insights from Bulk Rock Geochemistry and Remote Sensing Data Analysis. *Phys. Chem. Earth Parts A/B/C* **2024**, *133*, 103530. [CrossRef]
4. Saleh, G.M.; Kamar, M.S.; Khaleal, F.M.; Azer, M.K.; Nasr, T.; Lasheen, E.S.R. Petrogenesis and Tectonic Evolution of Tourmaline—Bearing Leucogranites, Sikait Area, Southeasten Desert of Egypt Utilizing Mineralogical and Bulk Rock Analysis. *Sci. Rep.* **2025**, *15*, 20191. [CrossRef] [PubMed]
5. Stern, R.J.; Ali, K. Crustal Evolution of the Egyptian Precambrian Rocks. In *The Geology of Egypt*; Hamimi, Z., El-Barkooky, A., Martínez Frías, J., Fritz, H., Abd El-Rahman, Y., Eds.; Regional Geology Reviews; Springer International Publishing: Cham, Switzerland, 2020; pp. 131–151, ISBN 978-3-030-15264-2.
6. Mokhtar, H.; Surour, A.A.; Azer, M.K.; Ren, M.; Said, A. Petrogenesis and Possible Fingerprints of the Najd Shear System on the Evolution of Deformed Granitic Rocks in the West Wadi Nugrus Area, Egypt. *J. Afr. Earth Sci.* **2023**, *207*, 105045. [CrossRef]
7. Bonin, B. A-Type Granites and Related Rocks: Evolution of a Concept, Problems and Prospects. *Lithos* **2007**, *97*, 1–29. [CrossRef]
8. Awad, H.A.; Zakaly, H.M.H.; Nastavkin, A.V.; El Tohamy, A.M.; El-Taher, A. Radioactive Mineralizations on Granitic Rocks and Silica Veins on Shear Zone of El-Missikat Area, Central Eastern Desert, Egypt. *Appl. Radiat. Isot.* **2021**, *168*, 109493. [CrossRef] [PubMed]

9. Awad, H.A.M.; Zakaly, H.M.H.; Nastavkin, A.V.; El-Taher, A. Radioactive Content and Radiological Implication in Granitic Rocks by Geochemical Data and Radiophysical Factors, Central Eastern Desert, Egypt. *Int. J. Environ. Anal. Chem.* **2022**, *102*, 7444–7457. [CrossRef]
10. El Dabe, M. New Occurrence of Polymetals Mineralized Pegmatites in The Older Granitoids, Wadi El Sheih Area, Central Eastern Desert, Egypt. *Al-Azhar Bull. Sci.* **2017**, *28*, 25–41. [CrossRef]
11. Fangary, I.H.; Orabi, A.M.; Tolba, A.S.; Abd Elghany, M.K.; Mohamed, L.A.E. Geology and Geochemistry of Neoproterozoic Basement Rocks at Um Had Area, Central Eastern Desert, Egypt. *Al-Azhar Bull. Sci.* **2024**, *35*, 9. [CrossRef]
12. Gaafar, M.; Ali, K. Geophysical and Geochemical Signature of Rare Metal Granites, Central Eastern Desert, Egypt: Implications for Tectonic Environment. *Al-Azhar Bull. Sci.* **2015**, *26*, 15–32. [CrossRef]
13. Hassaan, M.M.; Omar, S.A.; Khalil, A.E.; Shahin, T.M.; El-Naggar, I.M.; Sayyed, M.I.; Hanfi, M.Y. Prognostic Exploration of U-F-Au-Mo-W Younger Granites for Geochemical Pathfinders, Genetic Affiliations, and Tectonic Setting in El-Erediya-El-Missikat Province, Eastern Desert, Egypt. *Minerals* **2022**, *12*, 518. [CrossRef]
14. Lasheen, E.S.R.; Elyaseer, M.H.; Mohamed, W.H.; Azer, M.K.; Rashwan, M.A.; Thabet, I.A. Economic Feasibility of Gabal Um Takha Leucogranitic Intrusion, South Sinai, Egypt: Integrated Remote Sensing, Geochemical, Aeromagnetic, and Geotechnical Approach. *Phys. Chem. Earth Parts A/B/C* **2024**, *133*, 103531. [CrossRef]
15. Stern, R.J. Neoproterozoic Formation and Evolution of Eastern Desert Continental Crust—The Importance of the Infrastructure-Superstructure Transition. *J. Afr. Earth Sci.* **2018**, *146*, 15–27. [CrossRef]
16. Bentor, Y.K. The Crustal Evolution of the Arabo-Nubian Massif with Special Reference to the Sinai Peninsula. *Precambrian Res.* **1985**, *28*, 1–74. [CrossRef]
17. Lundmark, A.M.; Gabrielsen, R.H.; Austrheim, H.; Flaat, K.; Strand, T.; Ohm, S.E. Late Devonian Rifting in the Central North Sea: Evidence from Altered Felsic Volcanic Rocks in the Embla Oil Field. *Mar. Pet. Geol.* **2012**, *29*, 204–218. [CrossRef]
18. Azer, M.K.; Abdelfadil, K.M.; Asimow, P.D.; Khalil, A.E. Tracking the Transition from Subduction-related to Post-collisional Magmatism in the North Arabian–Nubian Shield: A Case Study from the Homrit Waggat Area of the Eastern Desert of Egypt. *Geol. J.* **2020**, *55*, 4426–4452. [CrossRef]
19. El-Awady, A.; Sami, M.; Abart, R.; Fathy, D.; Farahat, E.S.; Ahmed, M.S.; Osman, H.; Ragab, A. Petrogenesis and Tectonic Evolution of I- and A-Type Granites of Mount Abu Kibash and Tulayah, Egypt: Evidence for Transition from Subduction to Post-Collision Magmatism. *Minerals* **2024**, *14*, 806. [CrossRef]
20. Lasheen, E.S.R.; Abart, R.; Ahmed, M.S.; Abdelfadil, K.M.; Farahat, E.S.; Sami, M. Petrological Constraints of the Ediacaran Magmatic Intrusions, Homrit Mukpid Area, Southeastern Desert, Egypt: Bulk Rock Geochemistry and Mineralogy. *J. Afr. Earth Sci.* **2025**, *225*, 105567. [CrossRef]
21. Whalen, J.B.; Currie, K.L.; Chappell, B.W. A-Type Granites: Geochemical Characteristics, Discrimination and Petrogenesis. *Contrib. Mineral. Petrol.* **1987**, *95*, 407–419. [CrossRef]
22. Sami, M.; Ntaflos, T.; Mohamed, H.A.; Farahat, E.S.; Hauzenberger, C.; Mahdy, N.M.; Abdelfadil, K.M.; Fathy, D. Origin and Petrogenetic Implications of Spessartine Garnet in Highly-Fractionated Granite from the Central Eastern Desert of Egypt. *Acta Geol. Sin.-Engl. Ed.* **2020**, *94*, 763–776. [CrossRef]
23. Seddik, A.M.A.; Darwish, M.H.; Azer, M.K.; Asimow, P.D. Assessment of Magmatic versus Post-Magmatic Processes in the Mueilha Rare-Metal Granite, Eastern Desert of Egypt, Arabian-Nubian Shield. *Lithos* **2020**, *366–367*, 105542. [CrossRef]
24. Lasheen, E.S.R.; Rashwan, M.A.; Azer, M.K. Effect of Mineralogical Variations on Physico-Mechanical and Thermal Properties of Granitic Rocks. *Sci. Rep.* **2023**, *13*, 10320. [CrossRef] [PubMed]
25. Rashwan, M.A.; Lasheen, E.S.R.; Abdelwahab, W.; Azer, M.K.; Zakaly, H.M.H.; Alarifi, S.S.; Ene, A.; Thabet, I.A. Physico-Mechanical Properties and Shielding Efficiency in Relation to Mineralogical and Geochemical Compositions of Um Had Granitoid, Central Eastern Desert, Egypt. *Front. Earth Sci.* **2023**, *11*, 1228489. [CrossRef]
26. Saleh, G.M. *Uranium Mineralization in the Granitic Rocks of Nasb Aluba—Magal Gebriel Area, South Eastern Desert, Egypt*; Nuclear Material Authority: New Cairo, Egypt, 2001.
27. Deer, W.A.; Howie, R.A.; Zussman, J. *An Introduction to the Rock Forming Minerals*, 2nd ed.; Longman Scientific and Technical: London, UK, 1992.
28. Nachit, H.; Ibhi, A.; Abia, E.H.; Ben Ohoud, M. Discrimination between Primary Magmatic Biotites, Reequilibrated Biotites and Neoformed Biotites. *C. R. Geosci.* **2005**, *337*, 1415–1420. [CrossRef]
29. Miller, C.F.; Stoddard, E.F.; Bradfish, L.J.; Dollase, W.A. Composition of Plutonic Muscovite; Genetic Implications. *Can. Mineral.* **1981**, *19*, 25–34.
30. Monier, G.; Mergoil-Daniel, J.; Labernadière, H. Générations successives de muscovites et feldspaths potassiques dans les leucogranites du massif de Millevaches (Massif Central français). *Bull. Minéralogie* **1984**, *107*, 55–68. [CrossRef]
31. Clarke, D.B. The Mineralogy of Peraluminous Granites; a Review. *Can. Mineral.* **1981**, *19*, 3–17.

32. Leake, B.E.; Woolley, A.R.; Arps, C.E.S.; Birch, W.D.; Gilbert, M.C.; Grice, J.D.; Hawthorne, F.C.; Kato, A.; Kisch, H.J.; Krivovichev, V.G.; et al. Nomenclature of Amphiboles; Report of the Subcommittee on Amphiboles of the International Mineralogical Association Commission on New Minerals and Mineral Names. *Mineral. Mag.* **1997**, *61*, 295–310. [CrossRef]
33. Keeditse, M.; Rajesh, H.M.; Belyanin, G.A.; Fukuyama, M.; Tsunogae, T. Primary Magmatic Amphibole in Archaean Meta-Pyroxenite from the Central Zone of the Limpopo Complex, South Africa. *S. Afr. J. Geol.* **2016**, *119*, 607–622. [CrossRef]
34. Hawthorne, F.C.; Oberti, R.; Harlow, G.E.; Maresch, W.V.; Martin, R.F.; Schumacher, J.C.; Welch, M.D. Nomenclature of the Amphibole Supergroup. *Am. Mineral.* **2012**, *97*, 2031–2048. [CrossRef]
35. Hoskin, P.W.O.; Schaltegger, U. The Composition of Zircon and Igneous and Metamorphic Petrogenesis. *Rev. Mineral. Geochem.* **2003**, *53*, 27–62. [CrossRef]
36. Tindle, A.G.; Breaks, F.W. Columbite-Tantalite Mineral Chemistry from Rare-Element Granitic Pegmatites: Separation Lakeh Area, N.W. Ontario, Canada. *Mineral. Petrol.* **2000**, *70*, 165–198. [CrossRef]
37. Mahdy, N.M. Textural and Chemical Characteristics of Zircon, Monazite, and Thorite, Wadi Al-Baroud Area, Eastern Desert of Egypt: Implication for Rare Metal Pegmatite Genesis. *Ore Geol. Rev.* **2021**, *136*, 104225. [CrossRef]
38. Middlemost, E.A.K. Naming Materials in the Magma/Igneous Rock System. *Earth-Sci. Rev.* **1994**, *37*, 215–224. [CrossRef]
39. Streckeisen, A.L.; Le Maitre, R.W. A Chemical Approximation to the Modal QAPF Classification of the Igneous Rocks. *Neues Jahrb. Fur Mineral. Abh.* **1979**, *136*, 169–206.
40. Frost, B.R.; Frost, C.D. A Geochemical Classification for Feldspathic Igneous Rocks. *J. Petrol.* **2008**, *49*, 1955–1969. [CrossRef]
41. Sun, S.-S.; McDonough, W.F. Chemical and Isotopic Systematics of Oceanic Basalts: Implications for Mantle Composition and Processes. *Geol. Soc. Lond. Spec. Publ.* **1989**, *42*, 313–345. [CrossRef]
42. Yang, S.-Y.; Jiang, S.-Y.; Zhao, K.-D.; Jiang, Y.-H.; Ling, H.-F.; Luo, L. Geochronology, Geochemistry and Tectonic Significance of Two Early Cretaceous A-Type Granites in the Gan-Hang Belt, Southeast China. *Lithos* **2012**, *150*, 155–170. [CrossRef]
43. Hermann, A.G. Yttrium and lanthanides. In *Handbook of Geochemistry*; Springer: Berlin, Germany, 1970; pp. 57–71.
44. Irber, W. The Lanthanide Tetrad Effect and Its Correlation with K/Rb, Eu/Eu∗, Sr/Eu, Y/Ho, and Zr/Hf of Evolving Peraluminous Granite Suites. *Geochim. Cosmochim. Acta* **1999**, *63*, 489–508. [CrossRef]
45. Kawabe, I. Lanthanide Tetrad Effect in the Ln3+ Ionic Radii and Refined Spin-Pairing Energy Theory. *Geochem. J.* **1992**, *26*, 309–335. [CrossRef]
46. Anenburg, M.; Williams, M.J. Quantifying the Tetrad Effect, Shape Components, and Ce–Eu–Gd Anomalies in Rare Earth Element Patterns. *Math. Geosci.* **2022**, *54*, 47–70. [CrossRef]
47. Masuda, A.; Kawakami, O.; Dohmoto, Y.; Takenaka, T. Lanthanide Tetrad Effects in Nature: Two Mutually Opposite Types, W and M. *Geochem. J.* **1987**, *21*, 119–124. [CrossRef]
48. Jahn, B.; Wu, F.; Capdevila, R.; Martineau, F.; Zhao, Z.; Wang, Y. Highly Evolved Juvenile Granites with Tetrad REE Patterns: The Woduhe and Baerzhe Granites from the Great Xing'an Mountains in NE China. *Lithos* **2001**, *59*, 171–198. [CrossRef]
49. Basak, A.; Goswami, B. The Physico-Chemical Conditions of Crystallization of the Grenvillian Arfvedsonite Granite of Dimra Pahar, Hazaribagh, India: Constraints on Possible Source Regions. *Mineral. Petrol.* **2020**, *114*, 329–356. [CrossRef]
50. Watson, E.B.; Harrison, T.M. Zircon Saturation Revisited: Temperature and Composition Effects in a Variety of Crustal Magma Types. *Earth Planet. Sci. Lett.* **1983**, *64*, 295–304. [CrossRef]
51. Rudnick, R.L.; Gao, S. *Composition of the Continental Crust*; Elsevier: Amsterdam, The Netherlands, 2003; Volumes 3–9, ISBN 978-0-08-054807-4.
52. Fuhrman, M.L.; Lindsley, D.H. Ternary-Feldspar Modeling and Thermometry. *Am. Mineral.* **1988**, *73*, 201–215.
53. Henry, D.J. The Ti-Saturation Surface for Low-to-Medium Pressure Metapelitic Biotites: Implications for Geothermometry and Ti-Substitution Mechanisms. *Am. Mineral.* **2005**, *90*, 316–328. [CrossRef]
54. Uchida, E.; Endo, S.; Makino, M. Relationship Between Solidification Depth of Granitic Rocks and Formation of Hydrothermal Ore Deposits. *Resour. Geol.* **2007**, *57*, 47–56. [CrossRef]
55. Anderson, J.L.; Barth, A.P.; Wooden, J.L.; Mazdab, F. Thermometers and Thermobarometers in Granitic Systems. *Rev. Mineral. Geochem.* **2008**, *69*, 121–142. [CrossRef]
56. Anderson, J.L.; Smith, D.R. The Effects of Temperature and f_{O2} on the Al-in-Hornblende Barometer. *Am. Mineral.* **1995**, *80*, 549–559. [CrossRef]
57. Tuttle, O.F.; Bowen, N.L. *Geological Society of America Memoirs*; Geological Society of America: Boulder, CO, USA, 1958; Volume 74, pp. 1–146.
58. Nicolae, I.; Saccani, E. Petrology and Geochemistry of the Late Jurassic Calc-Alkaline Series Associated to Middle Jurassic Ophiolites in the South Apuseni Mountains (Romania). *Swiss Bull. Mineral. Petrol.* **2003**, *83*, 81–96.

59. Akinin, V.V.; Miller, E.L.; Wooden, J.L. Petrology and geochronology of crustal xenoliths from the Bering Strait Region: Linking deep and shallow processes in extending continental crust. In *Crustal Cross Sections from the Western North American Cordillera and Elsewhere: Implications for Tectonic and Petrologic Processes*; Geological Society of America: Boulder, CO, USA, 2009; ISBN 978-0-8137-2456-0.
60. Sylvester, P.J. Post-Collisional Alkaline Granites. *J. Geol.* **1989**, *97*, 261–280. [CrossRef]
61. Shand, S.J. *Eruptive Rocks*, 4th ed.; John-Wiley: New York, NY, USA, 1951.
62. Hassan, M.A.; Hashad, A.H. Precambrian of Egypt. In *The Geology of Egypt*; Said, R., Ed.; Balkema Publications: Rotterdam, The Netherlands, 1990; pp. 201–245.
63. Pearce, J.A.; Harris, N.B.W.; Tindle, A.G. Trace Element Discrimination Diagrams for the Tectonic Interpretation of Granitic Rocks. *J. Petrol.* **1984**, *25*, 956–983. [CrossRef]
64. Eby, G.N. Chemical Subdivision of the A-Type Granitoids: Petrogenetic and Tectonic Implications. *Geology* **1992**, *20*, 641. [CrossRef]
65. Grebennikov, A.V. *A*-Type Granites and Related Rocks: Petrogenesis and Classification. *Russ. Geol. Geophys.* **2014**, *55*, 1074–1086. [CrossRef]
66. Shaw, D.M. A Review of K-Rb Fractionation Trends by Covariance Analysis. *Geochim. Cosmochim. Acta* **1968**, *32*, 573–601. [CrossRef]
67. Creaser, R.A.; Price, R.C.; Wormald, R.J. A-Type Granites Revisited: Assessment of a Residual-Source Model. *Geology* **1991**, *19*, 163. [CrossRef]
68. Laurent, A.; Janoušek, V.; Magna, T.; Schulmann, K.; Míková, J. Petrogenesis and Geochronology of a Post-Orogenic Calc-Alkaline Magmatic Association: The Žulová Pluton, Bohemian Massif. *J. Geosci.* **2014**, *59*, 415–440. [CrossRef]
69. Liu, Y.; Zhang, L.; Santosh, M.; Dong, G.; Que, C.; Yang, C. Emplacement and Evolution of Zoned Plutons: Multiproxy Isotopic and Geochemical Evidence from the Peraluminous Laojunshan Leucogranite Suite, Southwestern China, and Implications on the Regional Geodynamic and Metallogenic History. *Gondwana Res.* **2023**, *116*, 89–103. [CrossRef]
70. Frost, B.R.; Barnes, C.G.; Collins, W.J.; Arculus, R.J.; Ellis, D.J.; Frost, C.D. A Geochemical Classification for Granitic Rocks. *J. Petrol.* **2001**, *42*, 2033–2048. [CrossRef]
71. Li, X.; Li, W.; Li, Z.-X. On the Genetic Classification and Tectonic Implications of the Early Yanshanian Granitoids in the Nanling Range, South China. *Chin. Sci. Bull.* **2007**, *52*, 1873–1885. [CrossRef]
72. Abdel-Rahman, A.-F.M.; El-Kibbi, M.M. Anorogenic Magmatism: Chemical Evolution of the Mount El-Sibai A-Type Complex (Egypt), and Implications for the Origin of within-Plate Felsic Magmas. *Geol. Mag.* **2001**, *138*, 67–85. [CrossRef]
73. Hora, J.M.; Singer, B.S.; Wörner, G.; Beard, B.L.; Jicha, B.R.; Johnson, C.M. Shallow and Deep Crustal Control on Differentiation of Calc-Alkaline and Tholeiitic Magma. *Earth Planet. Sci. Lett.* **2009**, *285*, 75–86. [CrossRef]
74. Cao, M.; Qin, K.; Li, G.; Evans, N.J.; Hollings, P.; Jin, L. Genesis of Ilmenite-Series I-Type Granitoids at the Baogutu Reduced Porphyry Cu Deposit, Western Junggar, NW-China. *Lithos* **2016**, *246–247*, 13–30. [CrossRef]
75. Taylor, S.R.; McLennan, S.M. *The Continental Crust: Its Composition and Evolution*; Stony Brook University: New York, NY, USA, 1985.
76. Kemp, A.I.S.; Hawkesworth, C.J.; Foster, G.L.; Paterson, B.A.; Woodhead, J.D.; Hergt, J.M.; Gray, C.M.; Whitehouse, M.J. Magmatic and Crustal Differentiation History of Granitic Rocks from Hf-O Isotopes in Zircon. *Science* **2007**, *315*, 980–983. [CrossRef] [PubMed]
77. Clemens, J. S-Type Granitic Magmas—Petrogenetic Issues, Models and Evidence. *Earth-Sci. Rev.* **2003**, *61*, 1–18. [CrossRef]
78. Sami, M.; Adam, M.M.A.; Lv, X.; Lasheen, E.S.R.; Ene, A.; Zakaly, H.M.H.; Alarifi, S.S.; Mahdy, N.M.; Abdel Rahman, A.R.A.; Saeed, A.; et al. Petrogenesis and Tectonic Implications of the Cryogenian I-Type Granodiorites from Gabgaba Terrane (NE Sudan). *Minerals* **2023**, *13*, 331. [CrossRef]
79. Soesoo, A. Fractional Crystallization of Mantle-derived Melts as a Mechanism for Some I-type Granite Petrogenesis: An Example from Lachlan Fold Belt, Australia. *JGS* **2000**, *157*, 135–149. [CrossRef]
80. Sami, M.; El Monsef, M.A.; Abart, R.; Toksoy-Köksal, F.; Abdelfadil, K.M. Unraveling the Genesis of Highly Fractionated Rare-Metal Granites in the Nubian Shield via the Rare-Earth Elements Tetrad Effect, Sr–Nd Isotope Systematics, and Mineral Chemistry. *ACS Earth Space Chem.* **2022**, *6*, 2368–2384. [CrossRef]
81. Barboni, M.; Bussy, F. Petrogenesis of Magmatic Albite Granites Associated to Cogenetic A-Type Granites: Na-Rich Residual Melt Extraction from a Partially Crystallized A-Type Granite Mush. *Lithos* **2013**, *177*, 328–351. [CrossRef]
82. Villaseca, C.; Orejana, D.; Paterson, B.A. Zr–LREE Rich Minerals in Residual Peraluminous Granulites, Another Factor in the Origin of Low Zr–LREE Granitic Melts? *Lithos* **2007**, *96*, 375–386. [CrossRef]
83. Burda, J.; Gawęda, A. Shear-Influenced Partial Melting in the Western Tatra Metamorphic Complex: Geochemistry and Geochronology. *Lithos* **2009**, *110*, 373–385. [CrossRef]
84. Williamson, B.J.; Downes, H.; Thirlwall, M.F.; Beard, A. Geochemical Constraints on Restite Composition and Unmixing in the Velay Anatectic Granite, French Massif Central. *Lithos* **1997**, *40*, 295–319. [CrossRef]

85. Ali, K.A.; Moghazi, A.-K.M.; Maurice, A.E.; Omar, S.A.; Wang, Q.; Wilde, S.A.; Moussa, E.M.; Manton, W.I.; Stern, R.J. Composition, Age, and Origin of the ~620 Ma Humr Akarim and Humrat Mukbid A-Type Granites: No Evidence for Pre-Neoproterozoic Basement in the Eastern Desert, Egypt. *Int. J. Earth Sci.* **2012**, *101*, 1705–1722. [CrossRef]
86. Farahat, E.S.; Mohamed, H.A.; Ahmed, A.F.; El Mahallawi, M.M. Origin of I- and A-Type Granitoids from the Eastern Desert of Egypt: Implications for Crustal Growth in the Northern Arabian–Nubian Shield. *J. Afr. Earth Sci.* **2007**, *49*, 43–58. [CrossRef]